Applied Physics Express 7, 041801 (2014)
http://dx.doi.org/10.7567/APEX.7.041801

Origin of anomalous anharmonic lattice dynamics of lead telluride

Takuma Shiga[1], Takuru Murakami[1], Takuma Hori[1], Olivier Delaire[2], and Junichiro Shiomi[1,3*]

[1]Department of Mechanical Engineering, The University of Tokyo, Bunkyo, Tokyo 113-8656, Japan
[2]Materials Science and Technology Division, Oak Ridge National Laboratory, Oak Ridge, TN 37831, U.S.A.
[3]Japan Science and Technology Agency, PRESTO, Kawaguchi, Saitama 332-0012, Japan

Received January 23, 2014; accepted February 18, 2014; published online March 11, 2014

The origin of the anomalous anharmonic lattice dynamics of lead telluride is investigated by molecular dynamics simulations with interatomic force constants (IFCs) obtained up to quartic terms from first principles. The calculations reproduce the asymmetry of the radial distribution function and the double peaks of transverse optical phonon previously observed with neutron diffraction and scattering experiments. They are identified to be due to the extremely large nearest-neighbor cubic IFCs in the [100] direction. The outstanding strength of the nearest-neighbor cubic IFCs, compared with the longer-range interactions, explains why the distortion in the radial distribution function is local.

Knowledge of the lattice anharmonicity, which is a source of intrinsic lattice thermal resistance, thermal expansion, and temperature dependence of elastic constant,[1,2] has recently become accessible with the development of numerical and experimental tools for probing anharmonic lattice dynamics. Lead telluride (PbTe) has been a popular material for studying lattice anharmonicity because it exhibits an intrinsically low lattice thermal conductivity (2.0–2.2 $\mathrm{W\,m^{-1}\,K^{-1}}$ at room temperature[3]), which is beneficial for thermoelectric applications.[4–8] Calculation of mode-dependent phonon scattering rate has revealed that heat conduction by longitudinal acoustic (LA) phonons is significantly inhibited by scattering with the strongly anharmonic transverse optical (TO) phonons.[7]

Further anomalous anharmonic characteristics of PbTe lattice dynamics have been experimentally observed in the radial distribution function from neutron diffraction[9] and the inelastic neutron scattering (INS) spectra.[10] The pair distribution function (PDF) for the nearest-neighboring Pb and Te atoms along the [100] direction obtained from the neutron diffraction experiments was found to deviate from a Gaussian distribution function with the deviation magnitude increasing with temperature.[9] In addition, it was emphasized that the nearest-neighboring peak in the PDF is surprisingly broad,[9] although it has long been known that PbTe exhibits large atomic displacement parameters (ADPs).[11] A more recent synchrotron X-ray powder diffraction experiment confirmed these large ADPs, and interpreted the synchrotron measurements in terms of Pb atoms that are off-centered from their equilibrium positions.[12] This would mean that the extent of off-centering increases with temperature unlike in the case of ferroelectric materials, such as perovskites, where the transition to paraelectric (displacive phase transition) occurs with increasing temperature.[1] However, models presented in Refs. 9 and 11 based on interpretations of the PDF and ADPs from diffraction experiments lead to a conclusion that is different from that in the studies of bond length based on measurements of the extended X-ray absorption fine structure (EXAFS), which showed that Pb atoms are not off-centered but undergo vibrations of large amplitude.[13,14] In addition, the asymmetry in PDF peaks has been reproduced by ab initio molecular dynamics simulations,[14,15] but these simulations also showed that there are no appreciable off-centerings nor local or global spontaneously broken symmetries at finite temperatures.[14,16]

The strong anharmonicity of PbTe is also manifested in the phonon dispersion relations. While the LA and TO phonon branches calculated using the harmonic theory[4,6,7] cross each other along the [100] crystallographic direction, INS experiments have identified that the LA-TO crossing is avoided (hereafter, avoided crossing)[10] at finite temperature. The experiment also found a peak emerging at the zone center with a frequency that is different from TO and longitudinal optical (LO) phonons, resulting in a *double peak* in the INS line shape. The shape of the double peak is strongly sensitive to temperature, suggesting that it originates from lattice anharmonicity.

The temperature dependence of the INS spectrum has been studied on the basis of the perturbation theory.[9] The self-consistent ab initio lattice dynamics (SCAILD)[17] method was used to calculate the temperature dependence of TO-phonon frequency at the zone center by modeling the anharmonicity using the quasi-harmonic theory.[2] The hardening of TO-phonon frequency with increasing temperature was qualitatively reproduced, although the emergence of the double peak features was not captured because the perturbation theory does not account for changes in the eigenstates.

In contrast, molecular dynamics (MD) methods can readily include changes in the eigenstates arising from lattice anharmonicity. In particular, the usability of the classical MD method for studying low-Debye-temperature materials such as PbTe has been greatly improved with the recent development of non-empirical force fields consisting of accurate anharmonic interatomic force constants (IFCs) obtained from first principles. The MD method with anharmonic IFCs has been shown to accurately reproduce the lattice thermal conductivity of pure and alloyed crystals.[18,19]

In this work, we have investigated the peak asymmetry in the radial distribution function, the avoided crossing in the dispersions, and the TO-mode double peak in crystalline PbTe using the classical MD method with first-principles-based anharmonic IFCs. IFCs are defined as the Taylor expansion coefficient of the potential energy (V) or interatomic force (F) with respect to the atomic displacement (u) around the equilibrium coordination:

$$F_i^\alpha = -\frac{\partial V}{\partial u_i^\alpha} = -\sum_{j,\beta} \Phi_{ij}^{\alpha\beta} u_j^\beta - \frac{1}{2!}\sum_{jk,\beta\gamma} \Psi_{ijk}^{\alpha\beta\gamma} u_j^\beta u_k^\gamma - \frac{1}{3!}\sum_{jkl,\beta\gamma\delta} \mathrm{X}_{ijkl}^{\alpha\beta\gamma\delta} u_j^\beta u_k^\gamma u_l^\delta, \quad (1)$$

where Φ, Ψ, and X are the harmonic, cubic, and quartic anharmonic IFCs, respectively. The subscripts i, j, k, and l are atomic indices, and the superscripts α, β, γ, and δ are Cartesian coordinates. The IFCs up to quartic term have been calculated using the *real-space displacement* method[20] with the Hellman–Feynman forces obtained by density-functional-theory calculations. The harmonic, cubic, and quartic IFCs were calculated considering the interaction up to sixth, first, and first neighboring atoms, respectively. More details of the calculation are described in previous reports.[7,18] Even when carefully stabilizing the MD simulation with quartic terms and random displacements described in Ref. 19, we were unable to realize stable MD simulations above 300 K, and thus, in this letter, we report results at temperatures lower than 300 K.

We first computed the radial distribution function $g(r)$ from the MD trajectories. MD simulations were typically performed for $4 \times 4 \times 4$ cubic supercells with 512 atoms. In each simulation, the trajectories were recorded for 600 ps with constant energy (i.e., microcanonical ensemble) after equilibration at a particular temperature. The time step was set to 2.0 fs. For each temperature, ten MD simulations with different initial conditions were performed and the calculated $g(r)$ was ensemble-averaged.

As shown in Fig. 1(a), the magnitude of the peaks in $g(r)$ decreases and the width of these peaks increases with increasing temperature. The first peak of $g(r)$, denoted hereafter as $g^{\text{1stPb-Te}}(r)$, is the radial distribution function of the distance between the nearest-neighboring Pb and Te atoms (along [100]). The figure shows that $g^{\text{1stPb-Te}}(r)$ exhibits an asymmetric non-Gaussian profile at higher temperatures. To clarify the trend, we used the Levenberg–Marquardt algorithm[21] to fit the $g^{\text{1stPb-Te}}(r)$ profiles by Gaussian distribution functions, as plotted in Figs. 1(b) and 1(c). It can be seen that $g^{\text{1stPb-Te}}(r)$ significantly deviates from the Gaussian distribution at a higher temperature (250 K), which agrees well with the ab initio MD simulations[14,15] and the experiment.[9] Here, we confirmed that, despite the distortion of $g^{\text{1stPb-Te}}(r)$ from the Gaussian distribution, the average position of the Pb atom is not off-centered, which is consistent with the ab initio MD simulation[14] and the EXAFS experiment.[13]

To quantify the temperature dependence of the peak asymmetry in $g^{\text{1stPb-Te}}(r)$, we calculated skewness and kurtosis through third- ($n = 3$) and fourth- ($n = 4$) order momenta of the distribution functions.

$$\text{Skewness} = \frac{m_3}{\sigma^3}, \quad \text{Kurtosis} = \frac{m_4}{\sigma^4} - 3,$$
$$m_n = \frac{\int_{r_p-R}^{r_p+R} dr (r-\mu)^n g^{\text{1stPb-Te}}(r)}{\int_{r_p-R}^{r_p+R} dr\, g^{\text{1stPb-Te}}(r)}, \tag{2}$$

where μ and σ denote the expectation and variance of $g^{\text{1stPb-Te}}(r)$, respectively. The integration is carried out from $r_p - R$ to $r_p + R$, where r_p is the distance of maximum $g^{\text{1stPb-Te}}(r)$. The constant R (= 0.6 Å) is set to be large enough to capture the entire peak. Skewness and kurtosis respectively quantify the asymmetry and flatness of the profile. Kurtosis is zero when the profile is Gaussian. Figures 1(d) and 1(e) show the temperature dependences of skewness and kurtosis of $g^{\text{1stPb-Te}}(r)$. For comparison, the values obtained from the radial distribution function of nearest-neighboring Pb (Te) and Pb (Te) atoms, located at approximately 4–5 Å, are also plotted. For the entire temperature range, the calculated

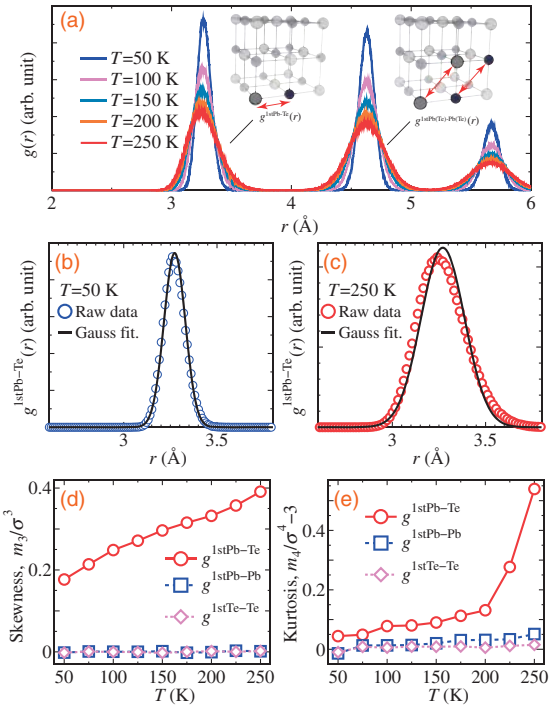

Fig. 1. (a) Radial distribution function $g(r)$ of pure PbTe crystal obtained by MD simulations at five different temperatures ($T = 50$, 100, 150, 200, and 250 K). (b, c) $g(r)$ of nearest-neighbor Pb–Te, $g^{\text{1stPb-Te}}(r)$, at $T = 50$ and 250 K, respectively. Open circles are the raw data, and the solid lines denote the Gaussian distribution functions fitted using the Levenberg–Marquardt algorithm.[21] (d, e) Temperature-dependent skewness and kurtosis of $g^{\text{1stPb-Te}}(r)$, $g^{\text{1stPb-Pb}}(r)$, and $g^{\text{1stTe-Te}}(r)$, respectively.

kurtosis values of $g^{\text{1stPb-Pb}}(r)$ and $g^{\text{1stTe-Te}}(r)$ are nearly zero, indicating that their profiles are Gaussian. In contrast, the deviation of $g^{\text{1stPb-Te}}(r)$ from the Gaussian distribution monotonically increases with temperature. Similarly, the positive value of skewness of $g^{\text{1stPb-Te}}(r)$ increases with temperature, indicating that the anharmonicity skews the profile towards a small distance (r). The linear trend of skewness is consistent with that of the extent of asymmetry measured in the experiments, although the dependence in the experiments became weak as the temperature exceeded 225 K.[9] In addition, it is interesting to note that the kurtosis of $g^{\text{1stPb-Te}}(r)$ exhibits a marked transition-like increase above 200 K, which may be worth investigating in more detail in the future.

We next calculated the dynamical structure factor[22,23] $S(\mathbf{Q}, \omega)$ for comparison with the INS experiments.[10,24]

$$S(\mathbf{Q}, \omega) = \frac{1}{2\pi N} \sum_{j,k} b_j b_k \int_{-\infty}^{\infty} dt \langle e^{-i\mathbf{Q}\cdot\mathbf{r}_j(0)} e^{i\mathbf{Q}\cdot\mathbf{r}_k(t)} \rangle, \tag{3}$$

where $\mathbf{Q}$, ω, and N are the wave vector, frequency, and total number of atoms in the system, respectively. The scattering length of jth atom b_j was set to 9.405×10^{-15} and 5.800×10^{-15} m for Pb and Te atoms, respectively.[23] The wave vector $\mathbf{Q}$ is the sum of the reciprocal lattice vector $\mathbf{G}$ and the phonon wave vector $\mathbf{q}$ ($\mathbf{Q} = \mathbf{G} + \mathbf{q}$). We chose (113) and (002) $\mathbf{G}$ vectors ($\mathbf{G}_{113}$ and $\mathbf{G}_{002}$) on the basis of the experiments.[10] For the $S(\mathbf{Q}, \omega)$ calculation, we performed MD simulations for a $10 \times 10 \times 10$ cubic supercell with 8,000 atoms to ensure that a sufficiently large number of wave vectors are allowed under the periodic boundary condition. In addition, ten 2.0-ns-long MD simulations were performed and ensemble-averaged to reduce the noise in $S(\mathbf{Q}, \omega)$.

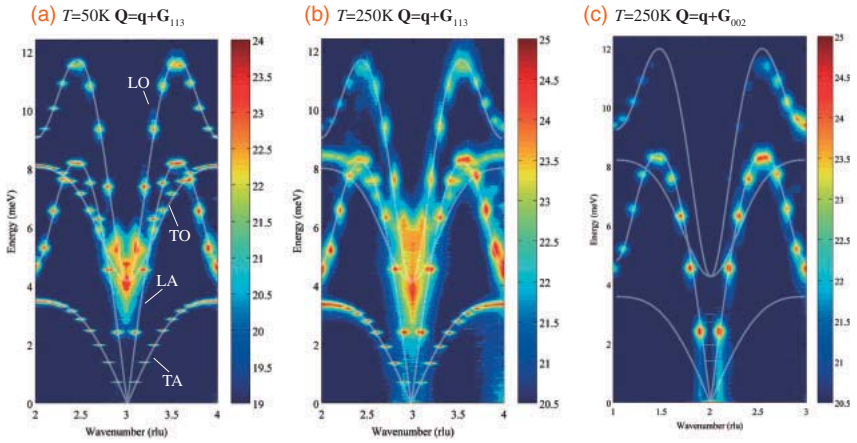

Fig. 2. Logarithmic contour plots of dynamical structure factor, $S(\mathbf{Q},\omega)$, along [001] symmetry line. (a, b) $S(\mathbf{Q},\omega)$ spectra for $\mathbf{Q}=\mathbf{q}+\mathbf{G}_{113}$ at $T=50$ and 250 K, respectively. (c) $S(\mathbf{Q},\omega)$ spectra for $\mathbf{Q}=\mathbf{q}+\mathbf{G}_{002}$ at $T=250$ K. White solid lines denote the phonon dispersion relations obtained by the harmonic lattice dynamics calculations.

Figure 2 shows $S(\mathbf{Q},\omega)$ calculated along the [001] crystallographic direction. White solid lines are phonon dispersion relations obtained by the harmonic lattice dynamics calculations. Here, note that the LO–TO splitting around the zone center[7,19] is absent because long-range interactions due to the ionic charge were not incorporated in the current MD simulations for simplicity. At a low temperature (50 K), as shown in Fig. 2(a), the peak positions of $S(\mathbf{Q},\omega)$ for the $\mathbf{Q}=\mathbf{q}+\mathbf{G}_{113}$ fall on the harmonic phonon dispersion relations except for the TO phonon modes around the zone center. Even at the higher temperature (250 K), the $S(\mathbf{Q},\omega)$ values of longitudinal phonon modes agree with the harmonic phonon dispersion relations, as shown in Fig. 2(b). On the other hand, transverse acoustic (TA) phonons become softer near the zone boundary, and the TO phonons become harder throughout the Brillouin zone. The hardening of TO phonons is consistent with the consequence of the avoided crossing observed in the experiments;[10] however, the extent of hardening here was insufficient to avoid the crossing. While peaks in $S(\mathbf{Q},\omega)$ for all the modes become broader as temperature increases owing to phonon scattering, the broadening and deformation of the optical phonon modes around the zone center are extraordinary, resulting in a spectrum that is completely different from the harmonic calculations. The *V shape* in the $S(\mathbf{Q},\omega)$ spectra around the zone center is in excellent agreement with the INS experiment.[10] The branch assignment of these optical phonon modes can be carried out by changing $\mathbf{G}$ from (113) to (002), where transverse modes in theory should be invisible. The absence of the extraordinarily broadened and deformed peaks in Fig. 2(c) indicates that these broad peaks are TO phonon modes.

Figure 3(a) shows the temperature dependence of the TO phonon modes at $\mathbf{G}_{113}$ in more detail. The presence of a double peak can be clearly identified. The frequency and line width of both peaks strongly depend on temperature, as observed in the INS experiments.[10,24] The two peaks were fitted by Gaussian distribution functions using the Levenberg–Marquardt algorithm,[21] and the obtained temperature dependences of the peak frequencies are plotted in Fig. 3(b). The frequency of the second peak increases with temperature, and the magnitude of change is larger than that of the first peak, which is consistent with the INS experiments.[10,24] Although there are still moderate discrepancies between the calculation and the experiments such as the sign of the slope of the first-peak frequency at approximately 100 K, overall, the classical MD simulations appear to capture the qualitative features of $S(\mathbf{Q},\omega)$ reasonably well.

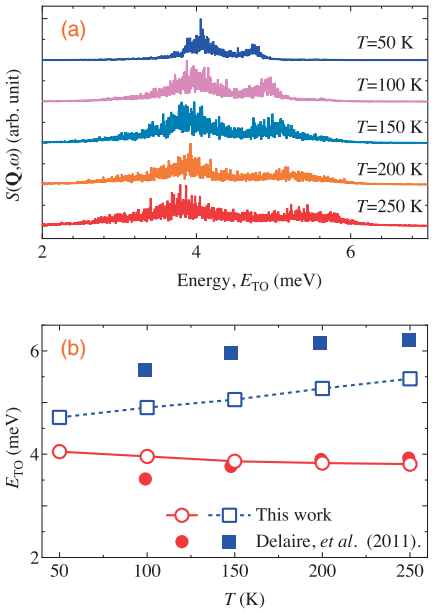

Fig. 3. (a) Temperature dependence of $S(\mathbf{Q},\omega)$ of TO mode at $\mathbf{Q}=\mathbf{G}_{113}$ calculated by MD simulations. (b) Temperature dependence of frequencies of the first and second peaks fitted by Gaussian using the Levenberg–Marquardt algorithm.[21] Filled circles and squares are the values from the INS experiment.[10]

We now identify which IFCs are responsible for the peak asymmetry in $g^{\text{1stPb-Te}}(r)$ and the double peak. It is intuitive to investigate the cubic anharmonic IFCs because they are asymmetric with respect to the atomic displacement. Considering the crystal symmetries of PbTe, there are in total six irreducible cubic IFCs, $\Psi_{ijk}^{\alpha\beta\gamma}$, as listed in Table I. The corresponding atomic displacements are shown in Fig. 4(a). The table shows a surprising feature that the first-nearest-neighbor cubic anharmonic IFCs along the [100] direction ($\Psi_{\text{PbTeTe}}^{zzz}$ and $\Psi_{\text{PbPbTe}}^{zzz}$) are more than 50 times larger than the others. We have also checked cubic IFCs up to third neighbors and confirmed that they are smaller than those of nearest neighbors. To determine the impact of the cubic IFCs on the line shape of the zone-center TO phonons, we performed additional simulations at 200 K using $\Psi_{\text{PbTeTe}}^{zzz}$ and $\Psi_{\text{PbPbTe}}^{zzz}$ with reduced magnitudes. The magnitudes were reduced in steps by scaling $\Psi_{\text{PbTeTe}}^{zzz}$ and $\Psi_{\text{PbPbTe}}^{zzz}$ with a factor η less than unity. As shown in Fig. 4(b), the magnitude of the double peak decreases as η decreases, and completely disappears as η approaches zero. Note that, in the case of $\eta=0$, the peak

Table I. Irreducible nearest-neighbor cubic anharmonic IFCs of PbTe crystal ($\Psi_{ijk}^{\alpha\beta\gamma}$). Pb and Te atoms in this table are located at $(0,0,0)$ and $(0,0,-1/2)a_{\mathrm{lat}}$, respectively, where a_{lat} denotes the lattice constants ($a_{\mathrm{lat}} = 6.548$ Å). The integers i, j, and k are atomic indices, and α, β, and γ are Cartesian coordinates.

No.	i	α	j	β	k	γ	$\Psi_{ijk}^{\alpha\beta\gamma}$ (eV/Å^3)
1	Pb	x	Pb	z	Te	x	−0.096
2	Pb	x	Pb	x	Te	z	−0.096
3	Pb	z	Pb	z	Te	z	5.599
4	Pb	z	Te	x	Te	x	0.096
5	Pb	x	Te	x	Te	z	0.096
6	Pb	z	Te	z	Te	z	−5.599

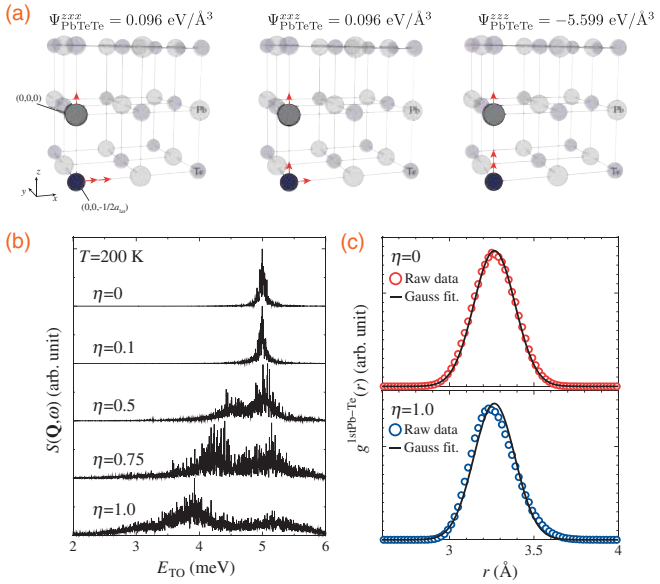

Fig. 4. (a) Atomic displacements corresponding to three cubic anharmonic IFCs ($\Psi^{zxx}_{\mathrm{PbTeTe}}$, $\Psi^{xxz}_{\mathrm{PbTeTe}}$, and $\Psi^{zzz}_{\mathrm{PbTeTe}}$) listed in Table I. Atoms at $(0,0,0)$ and $(0,0,-1/2)a_{\mathrm{lat}}$ are Pb and Te atoms, respectively. (b) $S(\mathbf{Q},\omega)$ spectra at $\mathbf{Q} = \mathbf{G}_{113}$ and 200 K calculated with the cubic anharmonic IFCs along the [001] direction ($\Psi^{zzz}_{\mathrm{PbTeTe}}$ and $\Psi^{zzz}_{\mathrm{PbPbTe}}$) scaled by a factor η. (c) $g^{1\mathrm{st}\mathrm{Pb}\text{-}\mathrm{Te}}(r)$ with $\eta = 0.0$ and 1.0 at 250 K. Open circles are the raw data, and the solid lines denote the Gaussian distribution functions fitted using the Levenberg–Marquardt algorithm.[21)]

frequency at 5 meV is 25% larger than that of the harmonic calculation owing to the anharmonicity of the other IFCs including the quartic ones. A similar parameter study was also carried out for the radial distribution function, and the distribution was found to become Gaussian by reducing the value of η to zero [Fig. 4(c)]. These results prove that it is indeed these nearest-neighbor cubic IFCs in the [100] direction that cause both the peak asymmetry in $g^{1\mathrm{st}\mathrm{Pb}\text{-}\mathrm{Te}}(r)$ and the double peak. In addition, the fact that the strongly anharmonic components of the cubic IFC tensor are confined to the nearest-neighbor bond explains why the distortion is limited to the nearest-neighbor peak in the radial distribution function. The fact that the large cubic IFCs give rise to the anharmonic lattice dynamics of TO phonons is consistent with the large three-phonon scattering rates of TO phonons,[7)] which is a cause of the low thermal conductivity of PbTe.

In summary, we have performed classical MD simulations of crystalline PbTe using IFCs up to quartic terms obtained from first principles. The radial distribution functions and dynamical structural factors calculated from the MD simulations qualitatively reproduce anomalous anharmonic-lattice-dynamics characteristics of PbTe such as peak asymmetry in $g^{1\mathrm{st}\mathrm{Pb}\text{-}\mathrm{Te}}(r)$ and double phonon peaks observed in neutron diffraction and inelastic scattering experiments, respectively. The anharmonic behavior originates from the extremely large nearest-neighbor cubic IFCs along the [100] direction. The outstanding strength of the nearest-neighbor cubic IFCs, compared with the longer-range interactions, also explains why the distortion of the radial distribution function is limited to a short range. In this work, we also demonstrate the usability of MD simulations with anharmonic IFCs for identifying the origin of anharmonic lattice dynamics, which may become useful for understanding and engineering old and new materials with preferred anharmonic thermodynamic properties.

Acknowledgments The authors are grateful to Dr. Gang Chen and Dr. Keivan Esfarjani for fruitful discussions. This work was partially supported by Research Fellowships of the Japan Society for the Promotion of Science for Young Scientists, Japan Science and Technology Agency PRESTO, Initiative on Promotion of Supercomputing for Young or Women Researchers, Supercomputing Division, Information Technology Center, The University of Tokyo, and KAKENHI 23760178.

1) H. Ibach and H. Lüth, *Solid-State Physics: An Introduction to Principles of Materials Science* (Springer, Heidelberg, 2003) p. 113.
2) J. M. Ziman, *Electrons and Phonons: The Theory of Transport Phenomena in Solids* (Oxford University Press, Oxford, U.K., 2000) p. 128.
3) H. J. Goldsmid, *Introduction to Thermoelectricity* (Springer, Heidelberg, 2009) p. 148.
4) W. Cochran, R. A. Cowley, G. Dolling, and M. M. Elcombe, Proc. R. Soc. London, Ser. A **293**, 433 (1966).
5) J. An, A. Subedi, and D. J. Singh, Solid State Commun. **148**, 417 (2008).
6) Y. Zhang, X. Ke, C. Chen, J. Yang, and P. R. C. Kent, Phys. Rev. B **80**, 024304 (2009).
7) T. Shiga, J. Shiomi, J. Ma, O. Delaire, T. Radzynski, A. Lusakowski, K. Esfarjani, and G. Chen, Phys. Rev. B **85**, 155203 (2012).
8) Z. Tian, J. Garg, K. Esfarjani, T. Shiga, J. Shiomi, and G. Chen, Phys. Rev. B **85**, 184303 (2012).
9) E. S. Božin, C. D. Malliakas, P. Souvatzis, T. Proffen, N. A. Spaldin, M. G. Kanatzidis, and S. J. L. Billinge, Science **330**, 1660 (2010).
10) O. Delaire, J. Ma, K. Marty, A. F. May, M. A. McGuire, M.-H. Du, D. J. Singh, A. Podlesnyak, G. Ehlers, M. D. Lumsden, and B. C. Sales, Nat. Mater. **10**, 614 (2011).
11) Y. Noda, K. Masumoto, S. Ohba, Y. Saito, K. Toriumi, Y. Iwata, and I. Shibuya, Acta Crystallogr., Sect. C **43**, 1443 (1987).
12) S. Kastbjerg, N. Bindzus, M. Søndergaard, S. Johnsen, N. Lock, M. Christensen, M. Takata, M. A. Spackman, and B. B. Iversen, Adv. Funct. Mater. **23**, 5477 (2013).
13) T. Keiber, F. Bridges, and B. C. Sales, Phys. Rev. Lett. **111**, 095504 (2013).
14) Y. Zhang, X. Ke, P. R. C. Kent, J. Yang, and C. Chen, Phys. Rev. Lett. **107**, 175503 (2011).
15) H. Kim and M. Kaviany, Phys. Rev. B **86**, 045213 (2012).
16) Y. Chen, X. Ai, and C. A. Marianetti, arXiv:1312.6109.
17) P. Souvatzis, O. Eriksson, M. I. Katsnelson, and S. P. Rudin, Comput. Mater. Sci. **44**, 888 (2009).
18) T. Murakami, T. Shiga, T. Hori, K. Esfarjani, and J. Shiomi, Europhys. Lett. **102**, 46002 (2013).
19) J. Shiomi, K. Esfarjani, and G. Chen, Phys. Rev. B **84**, 104302 (2011).
20) K. Esfarjani and H. T. Stokes, Phys. Rev. B **77**, 144112 (2008).
21) M. Wojdyr, J. Appl. Crystallogr. **43**, 1126 (2010).
22) G. L. Squires, *Introduction to the Theory of Thermal Neutron Scattering* (Dover, New York, 1978) p. 61.
23) G. Shirane, S. M. Shapiro, and J. M. Tranquada, *Neutron Scattering with a Triple-Axis Spectrometer: Basic Techniques* (Cambridge University Press, Cambridge, U.K., 2002) p. 233.
24) K. M. Ø. Jensen, E. S. Božin, C. D. Malliakas, M. B. Stone, M. D. Lumsden, M. G. Kanatzidis, S. M. Shapiro, and S. J. L. Billinge, Phys. Rev. B **86**, 085313 (2012).